

Gastric histopathology image segmentation using a hierarchical conditional random field

Changhao Sun^a, Chen Li^{a,*}, Xiaoyan Li^b

^aNortheastern University, Microscopic Image and Medical Image Analysis Group, MBIE College, Shenyang, P.R. China, 110819

^bChina Medical University, Department of Pathology, Cancer Hospital, Liaoning Cancer Hospital and Institute, Shenyang, P.R. China, 110042

Abstract. In this paper, a Hierarchical Conditional Random Field (HCRF) model based Gastric Histopathology Image Segmentation (GHIS) method is proposed, which can localize abnormal (cancer) regions in gastric histopathology images obtained by optical microscope to assist histopathologists in medical work. First, to obtain pixel-level segmentation information, we retrain a Convolutional Neural Network (CNN) to build up our pixel-level potentials. Then, in order to obtain abundant spatial segmentation information in patch-level, we fine-tune another three CNNs to build up our patch-level potentials. Thirdly, based on the pixel- and patch-level potentials, our HCRF model is structured. Finally, graph-based post-processing is applied to further improve our segmentation performance. In the experiment, a segmentation accuracy of 78.91% is achieved on a Hematoxylin and Eosin (H&E) stained gastric histopathological dataset with 560 images, showing the effectiveness and future potential of the proposed GHIS method.

Keywords: Image Segmentation, Gastric Cancer, Histopathology Image, Conditional Random Field, Convolutional Neural Network, Feature Extraction.

*Chen Li, lichen201096@hotmail.com

1 Introduction

Gastric Cancer is one of the five most common types of malignant tumors among men and women according to the World Health Organization (WHO). It represents 7% of all cases and 9% of all deaths among cancer patients. Almost 75% of new cases occur in Asia, and more than 40% occur in China.¹ The patients almost have 12 months of disease-specific survival and 90% of all cases dying within the first five years, meantime it is one of the most aggressive and deadliest cancer types. So, it is very important for medical professionals to accurately estimate patient prognoses.²

In recent years, Image Analysis plays a more and more important role in the intelligent diagnosis of gastric cancer, where a variety of Deep Learning (DL) methods, especially Convolutional Neural Networks (CNNs), are developed and applied to Gastric Histopathology Image Segmentation (GHIS) and classification tasks. From VGG-16³ to Fully Convolutional Networks (FCNs),⁴

from FCNs to DeepLab,⁵ the DL methods are constantly updated with the development of technology in the GHIS field. However, the existing approaches usually focus on individual characteristics and network framework, such as layer numbers and network structures, without a strategy to describe the integral information. Therefore, some advanced methods are proposed to integrate these individual existing methods to obtain an even better performance. Especially, because Conditional Random Fields (CRFs) can characterize the spatial relationship of images, they are effective and robust methods for analysing the contents of complex images. Whilst, due to medical doctors usually are too busy to draw all abnormal (cancer) regions, an effective multi-object segmentation approach is expected. Hence, we propose a Hierarchical Conditional Random Field (HCRF) model to address the GHIS problem, where the gastric histopathological images obtained by optical microscope are mixed with the complicated nucleus, interstitial and tissue fluid. Furthermore, because cellular visual features in a histopathological image can be observed on patch scales, when training the classifier, it is better to use the patches cut from the image than the whole image.⁶ The workflow of the proposed HCRF model is shown in Fig. 1, and the details are introduced in Sec. 3.

As shown in Fig. 1, we can see that: First, Data Input: To train the proposed HCRF model, original gastric carcinoma histopathological images (original images) and their corresponding ground truth images (GT images) are used as training and validation sets for a supervised learning process. The size of the original images is 2048×2048 pixels. The pixels in GT images are 1 (foreground abnormal regions, white) and 0 (background normal regions, black). Especially, some pre-processing is carried out: (1) In pixel-level training, we first augment the training and validation sets by flipping the original and GT images horizontally and vertically, and rotating the images to 90, 180, 270 degrees. Then we mesh the images into patches (256×256 pixels). (2)

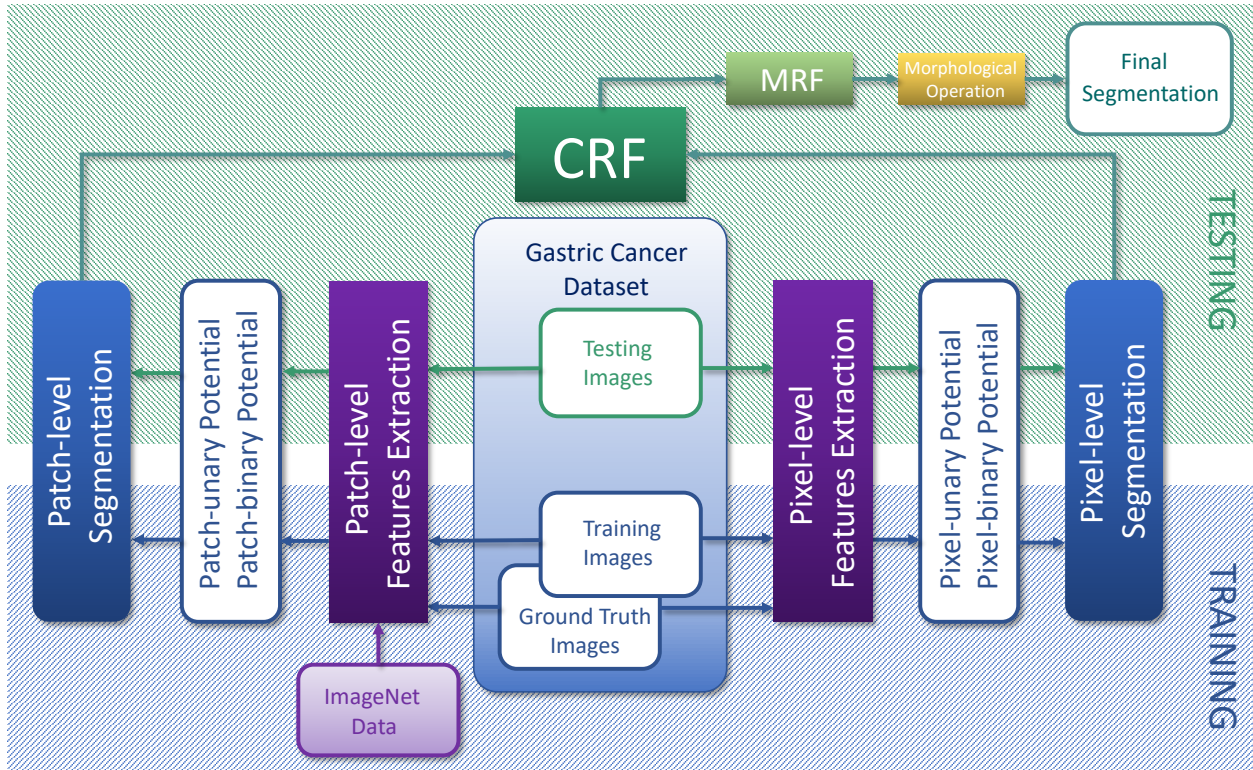


Fig 1 The workflow of the proposed hierarchical conditional random field (HCRF) model for the gastric histopathology image segmentation (GHIS).

In patch-level training, we mesh the original and GT images into patches (64×64 pixels) and the size of each patch is 4096 pixels. When the sum of the pixel values in a GT image is over 2048, we give the corresponding original image patch a foreground label (1, white); otherwise we give it a background label (0, black). However, when we do this approximate processing, the foreground image patches are much less than the background image patches. Hence, in order to balance the data during training, we specially augment the foreground image patches by flipping horizontally and vertically, and rotating the images to 90, 180, 270 degrees in the training and validation sets.

Second, HCRF Model: To build our HCRF based image segmentation model, we focus on four potentials, including pixel-unary, pixel-binary, patch-unary and patch-binary potentials. (1) In pixel-level, we extract pixel-level features and get the pixel-unary and pixel-binary segmentation results. (2) In patch-level, we first extract patch-level features and get three patch-unary and three

patch-binary segmentation results. Then, we obtain the optimized patch-unary and patch-binary segmentation results to enhance the segmentation performance. (3) Based on the pixel-unary, pixel-binary, patch-unary and patch-binary potentials, we generate the main body of our HCRF image segmentation model. (4) In addition, we apply Markov Random Field (MRF)⁷ and morphological operations⁸ to further optimize the segmentation result.

Third, System Evaluation: To evaluate the effectiveness of the proposed HCRF based image segmentation method, we input test images to it and calculate multiple indexes for an overall assessment.

There are three main contributions of our work: First, we heuristically apply a CRF framework to a research field of the GHIS. Second, we propose a HCRF model using higher order potentials in this paper. Thirdly, we obtain high segmentation performance by the HCRF model for gastric histopathology images.

The structure of this paper is as follows: Sec. 2 is the related work about this paper. Sec. 3 specifies how the HCRF model in this paper is designed. Sec. 4 gives experimental results of the proposed method. Finally, Sec. 5 closes this paper with a brief conclusion.

2 Related Work

In this section, the related works about this paper are summarized: Sec. 2.1 introduces related knowledge about gastric cancer; Sec. 2.2 discusses image segmentation techniques in gastric histopathology field; Sec. 2.3 is about the applications of CRFs; Sec. 2.4 concludes the related DL methods.

2.1 Gastric Cancer

Gastric cancer is the accumulation of an abnormal group of cells, either malignant or cancerous, which form a tumor in the stomach. Gastric cancer is situated in the third place after lung and breast cancer in women and second place after lung cancer in males. According to the data from WHO, nearly 800000 people die for the gastric cancer each year.⁹ Most of the gastric cancer cases occur in the Asia countries such as China and Japan. Especially in Japan, the number of people with gastric cancer occupies about 30% of other cancer diseases. In the Americas, the number of people with gastric cancer increases every year. The diagnosis of gastric cancer usually needs a careful examination of Hematoxylin and Eosin (H&E) stained tissue sections under a optical microscope by a pathologist. However, the microscopic examination of tissue sections is insipid, time-consuming, and may undergo subjectivity. In addition, the screening process usually takes 5–10 minutes for one slide. A pathologist cannot analyze more than 70 samples per day with a high work quality.¹⁰ This process also requires full attention at all times in case of missing any diagnostic cells. So, having a pathologist to screen and diagnose gastric cancer slides is a chief matter. With the rise and development of Artificial Intelligence (AI), more and more AI related methods are applied to the medical field,¹¹ making us to design an automated computerized system that can effectively and accurately analyse gastric cancer slides.¹²

2.2 Image Segmentation in Gastric Cancer Research

In,⁹ a multi-stage approach aims to segment the nuclei of gastric cancer from a histopathology image. First, a minimum-model method consisting of six main steps is used in the gastric cancer nuclei segmentation step. Then, color, texture and morphological features are extracted from the segmented nuclei. Thirdly, an ensemble learning method (multi-class AdaBoost classification al-

gorithm) is applied to improve the performance of individual classifiers. Lastly, the segmentation results at different resolutions are combined. In the experiment, to test the effectiveness of the proposed method, Her2/neu immunohistochemically stained and H&E stained surgical specimens of 12 cases (one specimen per case) are selected from 483 cases of gastric cancer. Finally, an average multi-class classification accuracy of 58.8% is achieved.

Recently, CNN-based methods are applied to gastric cancer segmentation. In,¹³ a three-class CNN is proposed to segment the inside, outside and the boundary of gastric cancer nuclei. First, color normalization is applied as a pre-processing step. Then, a three-class CNN is designed to emphasize the nuclear boundaries. Lastly, three classes of segmented objects are transferred to n -ary nuclear maps for post-processing. In the experiment, a large public accessible dataset of H&E stained tissue images with more than 21000 annotated nuclear boundaries is used for testing. This dataset is validated by a medical doctor and it covers seven organs, including breast, liver, kidney, prostate, bladder, colon and stomach. For each organ, there are 30 whole slide images (WSIs) in the dataset. Finally, average Dice's coefficient and F1-Score of 76.23% and 82.67% are obtained, respectively.

In,¹⁴ a U-Net based fully-connected network is proposed to detect nuclei and their boundaries at the same time from gastric histopathology image patches. In the experiment, three datasets are tested: The first is the same as that used in,¹³ and another two are breast cancer histopathology image datasets. Finally, 81.2%, 86.2%, 83% average Dice's coefficient, and 82.7%, 92.3% and 84%^a F1-Score are achieved on these three datasets, respectively.

2.3 Applications of Conditional Random Fields

Currently, conditional random fields (CRFs) are used in natural language processing or biological sequences¹⁵ and in computer vision¹⁶ areas for labelling or parsing of sequential data. Specifically, CRFs play roles in part-of-speech (POS) tagging, shallow parsing,¹⁷ named entity recognition,¹⁸ gene finding and peptide critical functional region finding,¹⁹ among other tasks, being an alternative to the related hidden Markov models (HMMs). In computer vision, CRFs are often used for image classification, image segmentation²⁰ and post-processing.⁵

In,²¹ a probabilistic discriminative method is proposed to fuse contextual constraints in functional images based on the CRFs and it is applied to the detection of brain activation from both synthetic and real fMRI data. The experimental results show that the proposed CRF approach validly integrates contextual constraints within the detection process and detects brain activities robustly from fMRI data.

In,²² a segmentation method is presented by combining CRFs with a cost-sensitive framework. Their experiment reveals that this method further improves its previous cost-sensitive SVM results by incorporating spatial information with the CRFs.

In,^{23,24} for extracting the domain-specific diagnostic features in probabilistic form, colposcopy images of cervical cancer neoplasia are used in a CRF framework. They judge and locate precancerous and cancerous areas based on the optical and tissue relationships of different tissues.

With the development of DL techniques, some works combine DL methods with CRF frameworks to obtain an even better classification and segmentation performance. For instance, in our previous work,²⁵ a microscopic image classification and segmentation engine that bases on DeepLab is proposed, which can automatically classify and segment the environmental microor-

ganism images using DL features in a strongly supervised CRF model. The experimental results shows 94.2% of overall segmentation accuracy and up to 91.4% mean average precision of the results. In our another work,²⁶ we design a weakly supervised multilayer hidden CRF framework with classical machine learning and DL techniques to classify gastric cancer images, achieving an overall accuracy of 93%. In this paper, we propose a HCRF framework with CNNs techniques for the gastric histopathology image segmentation (GHIS) task, which has not been applied to the problem in this field.

2.4 Related Deep Learning Method

VGG-16²⁷ contains 16 weight layers, including 13 convolution layers and 3 fully connected layers and 5 pooling layers without weights, and it uses convolution kernels with the same size to extract complex features.³ Inception-V3 network is based on the Inception-V1 and Inception-V2 networks. Inception-V1 contains inception module with dimension reduction using 1×1 convolution layers and multi-scale filters.²⁸ Inception-V2 further adds batch normalization into the network structure.²⁹ Inception-V3 factorizes the large convolutions into small convolutions and optimizes the Inception module.³⁰ Inception-V3 is more deeper than VGG-16 and uses multi-scale convolution kernels to extract multi-scale spatial features. In order to deal with the network degradation problem and train very deep neural networks, ResNet-50 proposes deep residual learning strategy using a short-cut connection structure.³¹ U-Net comes from FCNs, using “encode-decode” and “skip connection structures”.²⁷ As for seamless segmentation of optional large images, U-Net applies “overlap-tittle strategy”.²⁷ It shows effectiveness in medical image segmentation tasks, for example the works in.^{27,32,33}

3 Hierarchical Conditional Random Fields

In this section, the basic knowledge of CRFs is first introduced in Sec. 3.1. Then, the details of our HCRF model are proposed in Sec. 3.2, including pixel-unary, pixel-binary, patch-unary, patch-binary potentials, and their combination.

3.1 Basic Knowledge of CRFs

The definition of a conditional random field (CRF) is as follows:¹⁵ Firstly, \mathbf{Y} is defined as a random variable of the data sequence to be labelled, and \mathbf{X} is a random variable of the corresponding label sequence. Then, let $G = (V, E)$ be a graph such that $\mathbf{X} = (\mathbf{X}_v)_{v \in V}$, so that \mathbf{X} is indexed by the vertices (or nodes or points) of G . V is the array of all sites, corresponding to the nodes of an associated undirected graph $G = (V, E)$, whose edges E model interactions between adjacent sites. So, (\mathbf{X}, \mathbf{Y}) is a CRF in case, when conditioned on \mathbf{Y} , the random variables \mathbf{X}_v obey the Markov property with respect to the graph: $p(\mathbf{X}_v | \mathbf{Y}, \mathbf{X}_w, w \neq v) = p(\mathbf{X}_v | \mathbf{Y}, \mathbf{X}_w, w \sim v)$, where $w \sim v$ means that w and v are neighbours in G . This means that the CRF is an undirected graphical model whose nodes can be divided into two disjoint sets \mathbf{X} and \mathbf{Y} , which is the observed variable and the output variable. Then, the model conditional distribution is $p(\mathbf{X} | \mathbf{Y})$.

According to the basic theorem of the random fields in,³⁴ the joint distribution on the label sequence \mathbf{X} of a given \mathbf{Y} has the form as Eq. (1).

$$p_\theta(\mathbf{x} | \mathbf{y}) \propto \exp\left(\sum_{e \in E, k} \lambda_k f_k(e, \mathbf{x} |_e, \mathbf{y}) + \sum_{v \in V, k} \mu_k g_k(v, \mathbf{x} |_v, \mathbf{y})\right), \quad (1)$$

where \mathbf{y} is a data sequence, \mathbf{x} is a label sequence, and $\mathbf{x} |_S$ is the set of components of \mathbf{x} associated with the nodes in sub-graph S . Furthermore, from,^{35,36} it can be known that Eq. (1) can be rewritten

as Eq. (2).

$$p(\mathbf{X}|\mathbf{Y}) = \frac{1}{Z} \prod_C \psi_C(\mathbf{X}_C, \mathbf{Y}), \quad (2)$$

where $\psi_C(\mathbf{X}_C, \mathbf{Y})$ is the potential function on the clique C and $Z = \sum_{\mathbf{X}\mathbf{Y}} P(\mathbf{X}|\mathbf{Y})$ is the normalization factor. A clique, C , in an undirected graph $G = (V, E)$ is a subset of the vertices, $C \subseteq V$, such that every two distinct nodes are adjacent.

3.2 The Proposed HCRF Model

3.2.1 Structure of the HCRF Model

Most of CRF models have so far used only unary and binary potentials.^{5,36} However, potentials defined on higher order cliques have been shown to be useful in previous work, such as.^{37,38} Because we focus on the visual features of cellular scales in histopathological images,⁶ we introduce two types of higher order potentials, one is a patch-unary potential to represent the information of cells, and the other is a patch-binary potential to describe the surrounding spatial relationship among different cells. Hence, based on the basic definition of CRFs introduced in Sec. 3.1, our HCRF is expressed by Eq. (3).

$$p(\mathbf{X}|\mathbf{Y}) = \frac{1}{Z} \prod_{i \in V} \varphi_i(x_i; \mathbf{Y}; w_V) \prod_{(i,j) \in E} \psi_{(i,j)}(x_i, x_j; \mathbf{Y}; w_E) \prod_{m \in V_P} \varphi_m(\mathbf{x}_m; \mathbf{Y}; w_m; w_{V_P}) \prod_{(m,n) \in E_P} \psi_{(m,n)}(\mathbf{x}_m, \mathbf{x}_n; \mathbf{Y}; w_{(m,n)}; w_{E_P}), \quad (3)$$

where

$$Z = \sum_{\mathbf{X}\mathbf{Y}} \prod_{i \in V} \varphi_i(x_i; \mathbf{Y}) \prod_{(i,j) \in E} \psi_{(i,j)}(x_i, x_j; \mathbf{Y}) \prod_{m \in V_P} \varphi_m(\mathbf{x}_m; \mathbf{Y}) \prod_{(m,n) \in E_P} \psi_{(m,n)}(\mathbf{x}_m, \mathbf{x}_n; \mathbf{Y}), \quad (4)$$

is the normalization factor; V is the set of all nodes in the graph G , corresponding to the image pixels; E is the set of all edges in the graph G . V_P is one patch divided from an image; E_P represents the surrounding patches of a single patch. The usual clique potential function consists of two parts (terms): The pixel-unary potential function $\varphi_i(x_i, \mathbf{Y})$ is used to measure the probability that a pixel node i is labelled as $x_i \in \mathbf{X}$, which takes values from a given set of classes \mathbb{L} , for a given observation vector \mathbf{Y} ;²⁵ the pixel-binary potential function $\psi_{(i,j)}(x_i, x_j; \mathbf{X})$ is used to describe the adjacent nodes i and j in the graph. The spatial context relationship between them is related not only to the label of node i but also to the label of its neighbour node j . Furthermore, $\varphi_m(\mathbf{x}_m; \mathbf{Y})$ and $\psi_{(m,n)}(\mathbf{x}_m, \mathbf{x}_n; \mathbf{Y})$ are the newly introduced higher order potentials. The patch-unary potential function $\varphi_m(\mathbf{x}_m, \mathbf{Y})$ is used to measure the probability that a patch node m is labelled as \mathbf{x}_m for a given observation vector \mathbf{Y} ; the patch-binary potential function $\psi_{(m,n)}(\mathbf{x}_m, \mathbf{x}_n; \mathbf{Y})$ is used to describe the adjacent nodes m and n in the patch. w_V , w_E , w_{V_P} and w_{E_P} are the weights of the four potentials, $\varphi_i(x_i, \mathbf{Y})$, $\psi_{(i,j)}(x_i, x_j; \mathbf{X})$, $\varphi_m(\mathbf{x}_m, \mathbf{Y})$ and $\psi_{(m,n)}(\mathbf{x}_m, \mathbf{x}_n; \mathbf{Y})$, respectively. w_m and $w_{(m,n)}$ are the weights of the $\varphi_m(\cdot; \mathbf{Y})$ and $\psi_{(m,n)}(\cdot, \cdot; \mathbf{Y})$, respectively. These weights are used to find the largest posterior label $\tilde{\mathbf{X}} = \arg \max_{\mathbf{X}} p(\mathbf{X}|\mathbf{Y})$ and to further improve the image segmentation performance. To give a visualized understanding, the structure of our HCRF model is shown in Fig. 2.

In Fig. 2, the structure of our HCRF model is as follows:

- Layer I shows the real labels x_i of pixels and real labels \mathbf{x}_m of patches in an image.
- Layer II represents the original image pixels y_i which correspond one to one with the labels x_i , and the original image patches y_i which correspond one to one with the labels \mathbf{x}_m in Layer I.

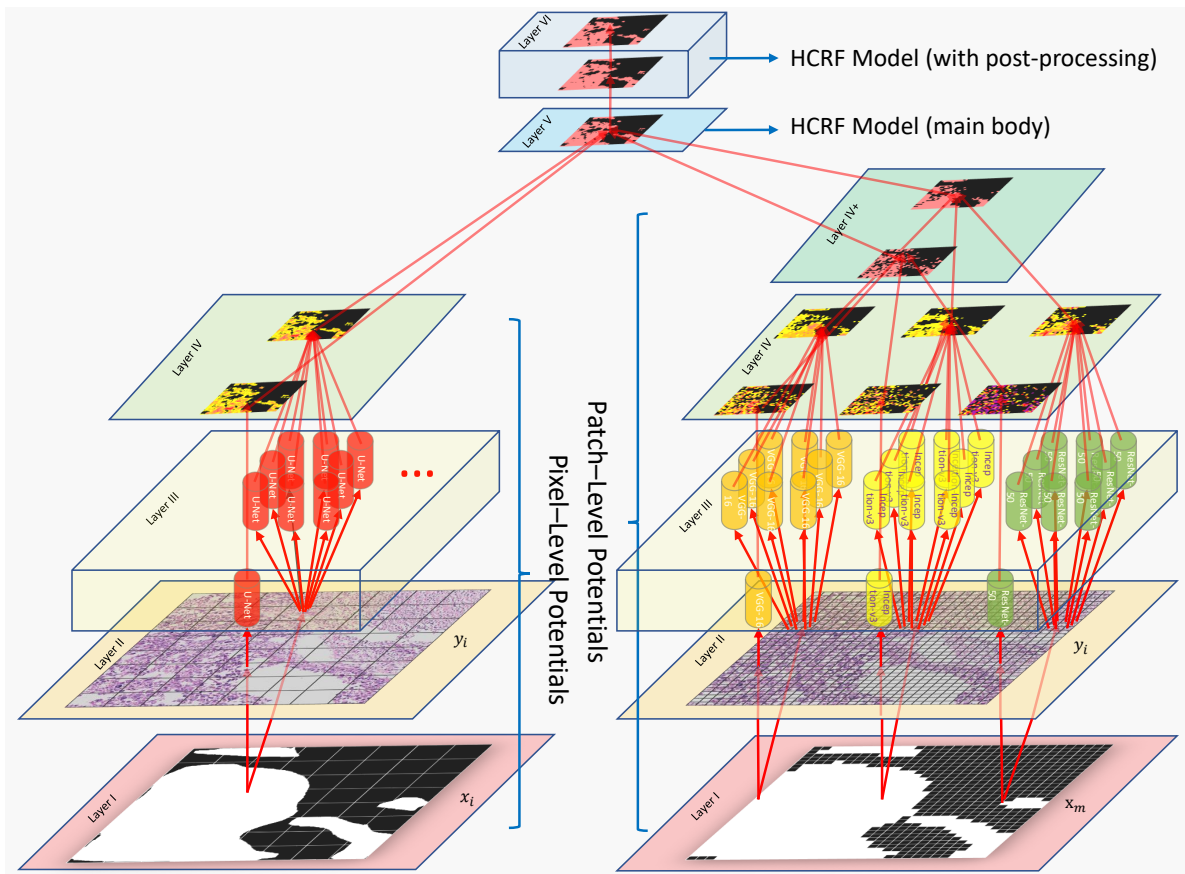


Fig 2 The structure of the proposed HCRF model. The left part denotes the terms of the pixel-level potentials, and the right part shows the terms of the patch-level potentials.

- From the pixel-level side, Layer III represents the U-Net, which is applied in pixel-level potentials using images pixels y_i . To this end, we retrain the U-Net using the gastric cancer histopathology images. From the patch-level side, Layer III denotes three types of CNNs that are applied in patch-level potentials using image patches y_i , including VGG-16, Inception-V3 and ResNet-50 networks. First, these three networks are pre-trained on 1.3 million images from ImageNet dataset³⁹ with a transfer learning strategy.^{3,4,40} Then, because the images from ImageNet are all natural and daily life pictures, we use the gastric cancer histopathology images to fine-tune the VGG-16, Inception-V3 and ResNet-50 networks.
- In Layer IV, we get one type of pixel-unary potential, corresponding to U-net; and three

types of patch-unary potentials, corresponding to VGG-16, Inception-V3 and ResNet-50 networks. In order to obtain the pixel-level binary potentials, we calculate the potentials of their surrounding image pixels according to the layout in Fig. 3. Similarly, to obtain the patch-level binary potentials, we calculate the potentials of their surrounding image patches according to the “lattice” layout in Fig. 4. Especially, there is an additional layer in the patch-level side, namely the Layer IV+, where we give weights w_m to the obtained three patch-unary potentials, respectively. To obtain the optimal combination of w_m , we iteratively calculate the three potentials to get the best patch-unary segmentation result. Similarly, we give weights $w_{(m,n)}$ to three patch-binary potentials to obtain an optimal patch-binary segmentation result.

- In Layer V, first, we give weights w_V and w_E to two obtained pixel-level potentials (pixel-unary and pixel-binary potentials), respectively; and give weights w_{VP} and w_{EP} to two obtained patch-level potentials (patch-unary and patch-binary potentials), respectively. Then, we calculate the joint probability of these four potentials to structure the final HCRF model.
- In Layer VI, in order to further improve the segmentation result from Layer V, we use MRF and morphological operations as post-processing in our work.

3.2.2 Pixel-unary Potential

The pixel-unary potential $\varphi_i(x_i; \mathbf{Y}; w_V)$ in Eq. (3) is related to the probability weights w_V of a label x_i , taking a value $c \in \mathbb{L}$ given the data Y by Eq. (5).

$$\varphi_i(x_i; \mathbf{Y}; w_V) \propto \left(p(x_i = c | f_i(Y)) \right)^{w_V}, \quad (5)$$

where the image data are conveyed by site-wise feature vector $f_i(Y)$ that may depend on all the data Y .⁴¹ The observation describes a pixel belonging to a gastric cancer region or to the background. Especially, considering the effectiveness of U-Net in medical image segmentation tasks, for $f_i(Y)$, we use $256 \times 256 \times 2$ -dimensional pixel-level feature F_i , obtaining feature maps at the penultimate convolution layer of the U-Net and the probability maps $p(x_i = c|f_i(Y))$ at the last convolution layer of the U-Net.²⁷ So, the pixel-unary potential is updated to Eq. (6).

$$\varphi_i(x_i; \mathbf{Y}; w_V) = \varphi_i(x_i; F_i; w_V), \quad (6)$$

where F_i depend on all the data Y .

3.2.3 Pixel-binary Potential

The pixel-binary potential $\psi_{(i,j)}(x_i, x_j; \mathbf{Y}; w_E)$ of the Eq. (3) conveys how similarly the pair of adjacent sites i and j is to take label $(x_i, x_j) = (c, c')$ given the data⁴¹ and weights, and it is defined as Eq. (7).

$$\psi_{(i,j)}(x_i, x_j; \mathbf{Y}; w_E) \propto \left(p(x_i = c; x_j = c' | f_i(Y), f_j(Y)) \right)^{w_E}. \quad (7)$$

In Fig. 3, the layout of our pixel-binary potential is shown. We use this ‘‘lattice’’ layout to describe the probability of each classified pixel by averaging each pixel of neighbourhood unary probability.²⁶ The other steps are consistent with the pixel-unary potential in Sec. 3.2.2.

3.2.4 Patch-unary Potential

In order to extract abundant spatial information, we choose VGG-16, Inception-V3 and ResNet-50 networks to extract patch-level features. In patch-level terms, we use α, β, γ to represent VGG-16,

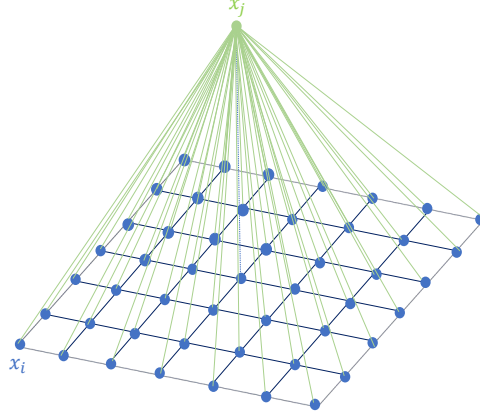


Fig 3 48 neighbourhood “Lattice” layout of the pixel-binary potential. The average of the unary probabilities of the 48 neighbourhood pixels is used as the probability of the pixel (the central pixel in green).

Inception-V3 and ResNet-50 networks, respectively. In patch-unary potentials $\varphi_m(\mathbf{x}_m; \mathbf{Y}; w_m; w_{VP})$ of Eq. (3), label $\mathbf{x}_m = \{x_{(m,\alpha)}, x_{(m,\beta)}, x_{(m,\gamma)}\}$ and $w_m = \{w_{(m,\alpha)}, w_{(m,\beta)}, w_{(m,\gamma)}\}$. $\varphi_m(\mathbf{x}_m; \mathbf{Y}; w_m; w_{VP})$ are related to the probability of labels $(w_{(m,\alpha)}, w_{(m,\beta)}, w_{(m,\gamma)}) = (c, c, c)$ given the data Y by Eq. (8).

$$\begin{aligned} \varphi_m(\mathbf{x}_m; \mathbf{Y}; w_m; w_{VP}) &\propto \left((p(x_{(m,\alpha)} = c | f_{(m,\alpha)}(Y)))^{w_{(m,\alpha)}} \right. \\ &\left. (p(x_{(m,\beta)} = c | f_{(m,\beta)}(Y)))^{w_{(m,\beta)}} (p(x_{(m,\gamma)} = c | f_{(m,\gamma)}(Y)))^{w_{(m,\gamma)}} \right)^{w_{VP}}, \end{aligned} \quad (8)$$

where the image data are conveyed by site-wise feature vectors $f_{(m,\alpha)}(Y)$, $f_{(m,\beta)}(Y)$ and $f_{(m,\gamma)}(Y)$ that may depend on all the data Y . For $f_{(m,\alpha)}(Y)$, $f_{(m,\beta)}(Y)$, and $f_{(m,\gamma)}(Y)$, we use 1024-dimensional patch-level bottleneck features $F_{(m,\alpha)}$, $F_{(m,\beta)}$ and $F_{(m,\gamma)}$, obtained from pre-trained VGG-16, Inception-V3 and ResNet-50 by ImageNet; and retrain their last three fully connected layers⁴² using gastric histopathology images to obtain the classification probability of each class. So, the patch-unary potential is updated to Eq. (9).

$$\varphi_m(\mathbf{x}_m; \mathbf{Y}; w_m; w_{VP}) = \varphi_m(\mathbf{x}_m; F_{(m,\alpha)}; F_{(m,\beta)}; F_{(m,\gamma)}; w_m; w_{VP}), \quad (9)$$

where $F_{(m,\alpha)}$, $F_{(m,\beta)}$ and $F_{(m,\gamma)}$ depend on all the data Y .

3.2.5 Patch-binary potential functions

The patch-binary potential $\psi_{(m,n)}(\mathbf{x}_m, \mathbf{x}_n; \mathbf{Y}; w_{(m,n)}; w_{EP})$ of the Eq. (3) denotes how similarly the pair of adjacent patch sites m and n is to take label $(\mathbf{x}_m, \mathbf{x}_n) = (c, c')$ given the data and weights, and it is defined as Eq. (10).

$$\begin{aligned} \psi_{(m,n)}(\mathbf{x}_m, \mathbf{x}_n; \mathbf{Y}; w_{(m,n)}; w_{EP}) \propto & \\ & \left((p(\mathbf{x}_{(m,\alpha)} = c; \mathbf{x}_{(n,\alpha)} = c' | f_{(m,\alpha)}(Y), f_{(n,\alpha)}(Y)))^{w_{(m,n,\alpha)}} \right. \\ & (p(\mathbf{x}_{(m,\beta)} = c; \mathbf{x}_{(n,\beta)} = c' | f_{(m,\beta)}(Y), f_{(n,\beta)}(Y)))^{w_{(m,n,\beta)}} \\ & \left. (p(\mathbf{x}_{(m,\gamma)} = c; \mathbf{x}_{(n,\gamma)} = c' | f_{(m,\gamma)}(Y), f_{(n,\gamma)}(Y)))^{w_{(m,n,\gamma)}} \right)^{w_{EP}}, \end{aligned} \quad (10)$$

where $\mathbf{x}_n = \{\mathbf{x}_{(n,\alpha)}, \mathbf{x}_{(n,\beta)}, \mathbf{x}_{(n,\gamma)}\}$ denotes the patch labels and $w_{(m,n)} = \{w_{(m,n,\alpha)}, w_{(m,n,\beta)}, w_{(m,n,\gamma)}\}$ represents the patch weights. We use the “lattice” layout in Fig. 4 to calculate the probability of each classified patch by averaging each patch of neighbourhood unary probability.²⁶ The other operations are similar to the patch-binary potential in Sec. 3.2.4.

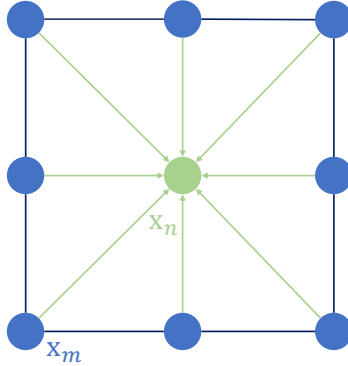


Fig 4 Eight neighbourhood “Lattice” layout of the patch-binary potential. The average of unary probabilities of the eight neighbourhood patches is used as the probability of the target patch (the central patch ingreen).

4 Experiments

4.1 Experimental Setting

4.1.1 Image Dataset

In this paper, we use a H&E stained gastric histopathological image dataset⁴³ to test the effectiveness of our proposed HCRF model in the gastric histopathology image segmentation (GHIS) task.

The details of this applied dataset are as follows:

- Data source: A public dataset. Practical histopathologists mark most of the abnormal regions in histopathology images of gastric cancer.
- Staining method: H&E Staining.
- Magnification: 20×.
- Image size: 2048 × 2048 pixels.
- Image format: “*.tiff” or “*.png”.
- Image type: Normal images, no positive regions (cancerous cells) appear in the sections; abnormal images, positive regions appear in the sections; ground truth images (GT images), the positive regions are labelled in the sections.
- Image number: 140 normal images without GT images, and 560 abnormal images with 560 GT images.

An example of this applied gastric H&E dataset is shown in Fig. 5.

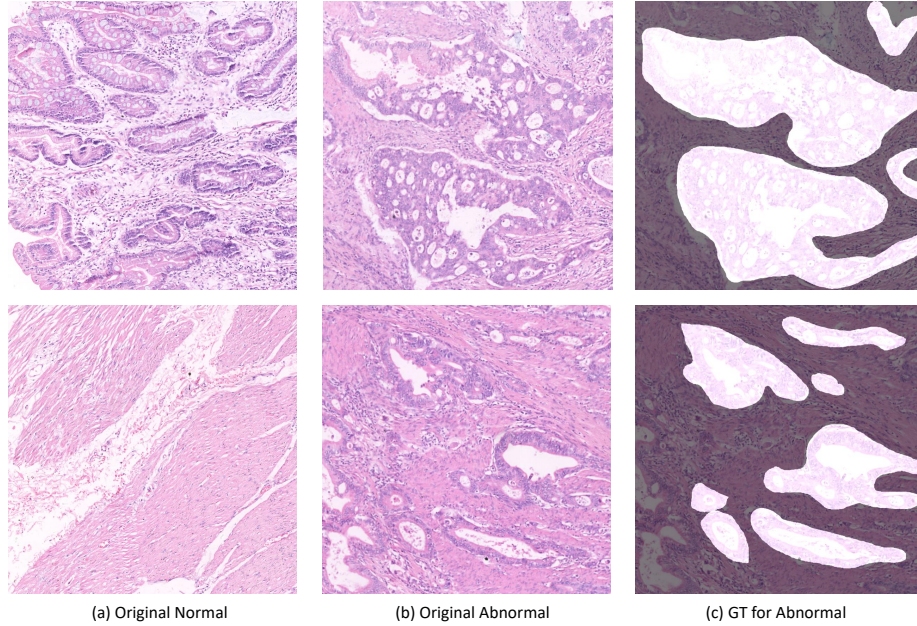


Fig 5 An example of the H&E staining gastric histopathological image dataset. The right column shows the original images of normal tissues, the original images in the middle column contain abnormal regions, and the left column shows the corresponding GT images of the abnormal regions in the middle column. In the GT images, the brighter regions are positive (abnormal tissues with cancer cells), and the darker regions are negative (normal tissues without cancer cells).

4.1.2 Training, Validation and Test Data Setting

In the GHIS task, we only use the 560 abnormal images and their corresponding GT images from the gastric histopathological image dataset. The abnormal images are randomly divided into training, validation and test sets with a ratio of 1:1:2. The data setting is shown in Table 1.

Table 1 Experimental data setting with the abnormal type. The first column shows the image type. The second to the fourth columns show different usage of the data, respectively. The last column shows the total number of images used in this paper.

Imge tpye	Training	Validation	Test	Sum
Original images	140	140	280	560

In the pixel-level potentials, we flip the original and GT images horizontally and vertically and rotate them 90, 180, 270 degrees to augment the training and validation datasets 6 times. Furthermore, because the size of the gastric histopathology images is too large to process, we crop

the original and the GT images into 256×256 pixels. The data augmentation for the pixel-level training is shown in Table 2.

Table 2 Data augmentation for training and validation sets in pixel-level training. The first column shows the image types. The second and third columns show usage of data, respectively. The last column is the total number of images used in this paper.

Image type	Training	Validation	Sum
Original images	140	140	280
Augmented images	53760	53760	107520

In the patch-level potential, we mesh the original and GT images into patches (64×64 pixels) and the area of a patch is 4096 pixels. When the sum of the pixel numbers in a GT image is over 2048, we give a positive label (1, foreground) to the corresponding original image patch; otherwise, we give it a negative label (0, background). However, when we do this operation, the positive image patches are much less than the negative image patches. So, in order to balance the data during training, we augment the positive image patches by flipping horizontally and vertically and rotating them to 90, 180, 270 degrees in the training set. Meantime, we do the same augmentation to the images in the validation set. The data augmentation for the patch-level is shown in Table 3.

Table 3 Data augmentation for training and validation sets in patch-level training. The first column shows the image types. The second to the third columns show usage of data, respectively. The bottom row is the total number of images used in this paper.

Image type	Train	Validation
Augmented positive images	121251	119151
Augmented negative images	121251	119151
Sum	242502	238302

4.2 Evaluation of Pixel-level Potentials

4.2.1 Evaluation Methods

First, we use the training and validation sets in Table 2 to train the U-Net. The validation set is used to tune the CNN parameters and avoid the CNN overfitting or underfitting during the training process. Second, we obtain the prediction probability of each pixel in an image in validation and test sets. Thirdly, in order to evaluate the segmentation performance, we split joint the 256×256 pixel images to 2048×2048 pixel images, and use 140 validation images of 2048×2048 pixels and 280 test images of 2048×2048 pixels to evaluate the segmentation result. To give a quantitative evaluation, we use Sørensen-Dice coefficient (Dice or F1-score), Relative Volume Difference (RVD), Intersection over Union (IoU or Jaccard), Precision (or positive predictive value), Recall (or sensitivity), Specificity (or true negative rate) and Accuracy to measure the segmentation result, where these criteria are common and suitable for medical image segmentation evaluation.⁴⁴⁻⁴⁷

These seven criteria are defined in Table 4.

Table 4 The seven evaluation criteria and corresponding definitions.

Criterion	Definition	Criterion	Definition
Dice	$\frac{2TP}{2TP + FP + FN}$	Recall	$\frac{TP}{TP + FN}$
RVD	$ \frac{FP + TP}{TP + FN} - 1$	Specificity	$\frac{TN}{TN + FP}$
IoU	$\frac{TP}{TP + FN + FP}$	Accuracy	$\frac{TP + TN}{TP + FN + TN + FP}$
Precision	$\frac{TP}{TP + FP}$		

where TP is the True Positive (positive sample is predicted to be positive), TN is the True Negative (negative sample is predicted to be negative), FP is the False Positive (negative sample is predicted to be positive), and FN is the False Negative (positive sample is predicted to be negative).

Dice is in the interval $[0,1]$, and a perfect segmentation yields a Dice of 1. RVD is an asymmetric metric, and a lower RVD means a better segmentation result.⁴⁷ IoU is the standard metric for segmentation purposes that computes a ratio between the intersection and the union of two sets, and a high IoU means a better segmentation result.⁴⁴ Precision is the fraction of relevant instances among the retrieved instances, where a high precision means that an algorithm returns substantially more relevant results than irrelevant ones. Recall is the fraction of relevant instances that have been retrieved over the total amount of relevant instances, where a high recall means that an algorithm returns most of the relevant results. Specificity measures the proportion of actual negatives that are correctly identified as such.⁴⁸ Accuracy is the correct predicted pixels among the whole pixels, where a high accuracy means a better segmentation result.

4.2.2 Evaluation for Pixel-level Segmentation Results

From Fig. 6, we can see an example of the segmentation results on the validation set, where we use different colors to describe different predicted probabilities. The probabilities are the higher, the regions have a greater risk to contain cancer tissues inside. The black, yellow, orange, tomato, red and purple colors represent the probabilities between $[0, 0.5)$, $[0.5, 0.6)$, $[0.6, 0.7)$, $[0.7, 0.8)$, $[0.8, 0.9)$ and $[0.9, 1]$, respectively.

The original images in Fig. 6 are common and representative cases in our GHIS work, so we choose them as visible comparison in this paper. We can find that the pixel-binary potential results remove some noise that appears in the pixel-unary potential results, showing a stronger denoising ability. However, because the binary-pixel potential makes some correctly classified pixel in the pixel-unary potential go wrong, the pixel-unary potential still makes sense in our HCRF model with a complementarity to the pixel-binary potential. Meanwhile, the evaluation indexes are show

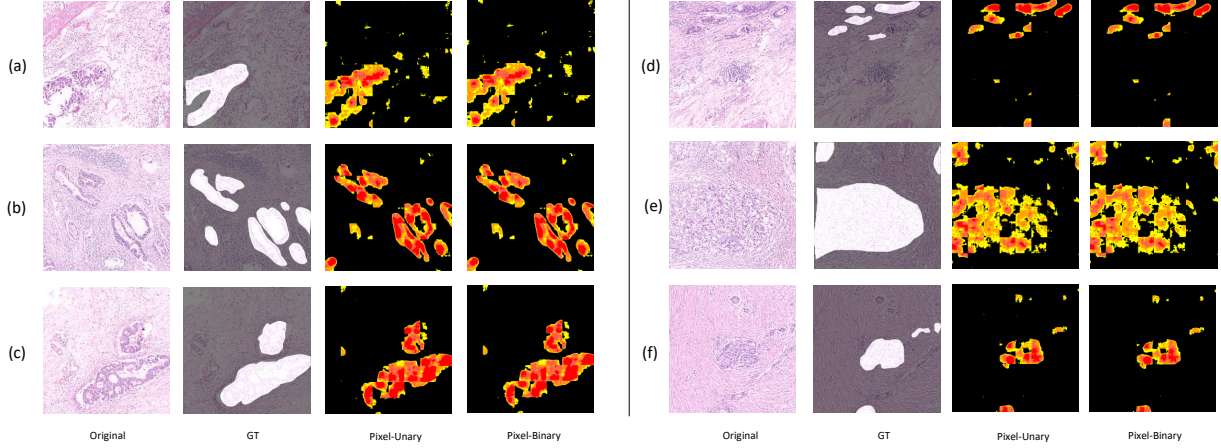


Fig 6 An example of the pixel-level segmentation result on the validation set. The first and second columns show the original and their GT images, respectively. The third and last columns are the image segmentation results with pixel-unary and pixel-binary potentials, respectively. (a) is an image with a single abnormal region; (b) and (c) are examples for multiple abnormal regions; (d) represents the case with very small abnormal regions; (e) is an example with a very big abnormal region; (f) shows an un conspicuous case of abnormal regions.

in Fig. 7.

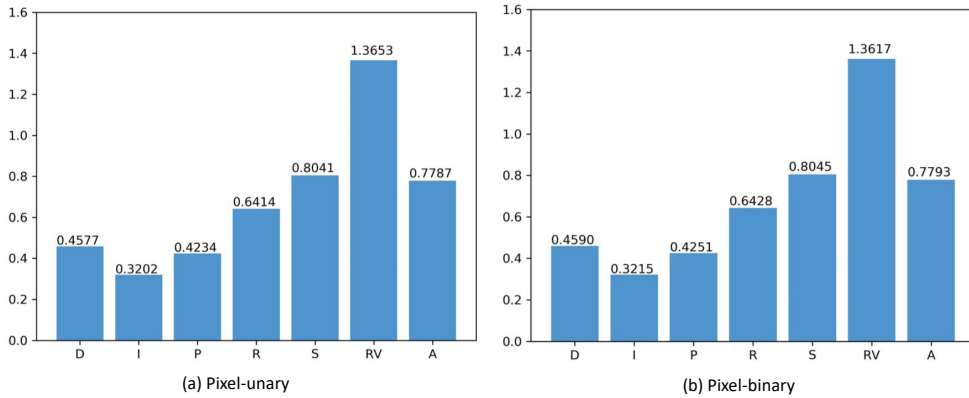


Fig 7 The evaluation for the image segmentation performance of the pixel-level potentials on the validation set. (a) and (b) are the evaluations of pixel-unary and pixel-binary potentials on the validation set, respectively. D, I, P, R, S, RV and A represent Dice, IoU, Precision, Recall, Specificity, RVD and Accuracy, respectively.

4.3 Evaluation of Patch-Level Potentials

4.3.1 Evaluation for Patch-level Segmentation Results

First, we train the VGG-16, Inception-V3 and ResNet-50 networks separately, using the training and validation sets in Table 3. Then, we get the label and predicted probability of each image patch.

The classification accuracy of 238302 image patches in the validation set is shown in Table 5.

Table 5 Classification accuracies of three CNNs on the validation set in patch-level training. The first column shows the different patch-level potentials. The second to the last columns show different CNNs.

Potentials	VGG-16	Inception-V3	ResNet-50
Patch-unary	0.7226	0.6889	0.7118
Patch-binary	0.7331	0.7139	0.7494

From Table 5, we can find that the VGG-16 performs well both in the patch-unary and -binary potentials, showing a strong feature extraction ability of this network model in the histopathology image analysis work. Furthermore, the classification confusion matrices are shown in Fig. 8.



Fig 8 Image patch classification results of three CNNs on the validation set. The left, middle and right columns represent the confusion matrices for the classification results of VGG-16, Inception-V3 and ResNet-50 networks of patch-unary and -binary potentials, respectively, where 1 represents positive and 0 represents negative.

Furthermore, in order to visualize the classification results, we piece together the patches and obtain the patch-level segmentation results, including three patch-unary results and three patch-binary results in Fig. 9. The probabilities of image patches corresponding to colors are set as the same as the pixel-level potentials in Sec. 4.2.2.

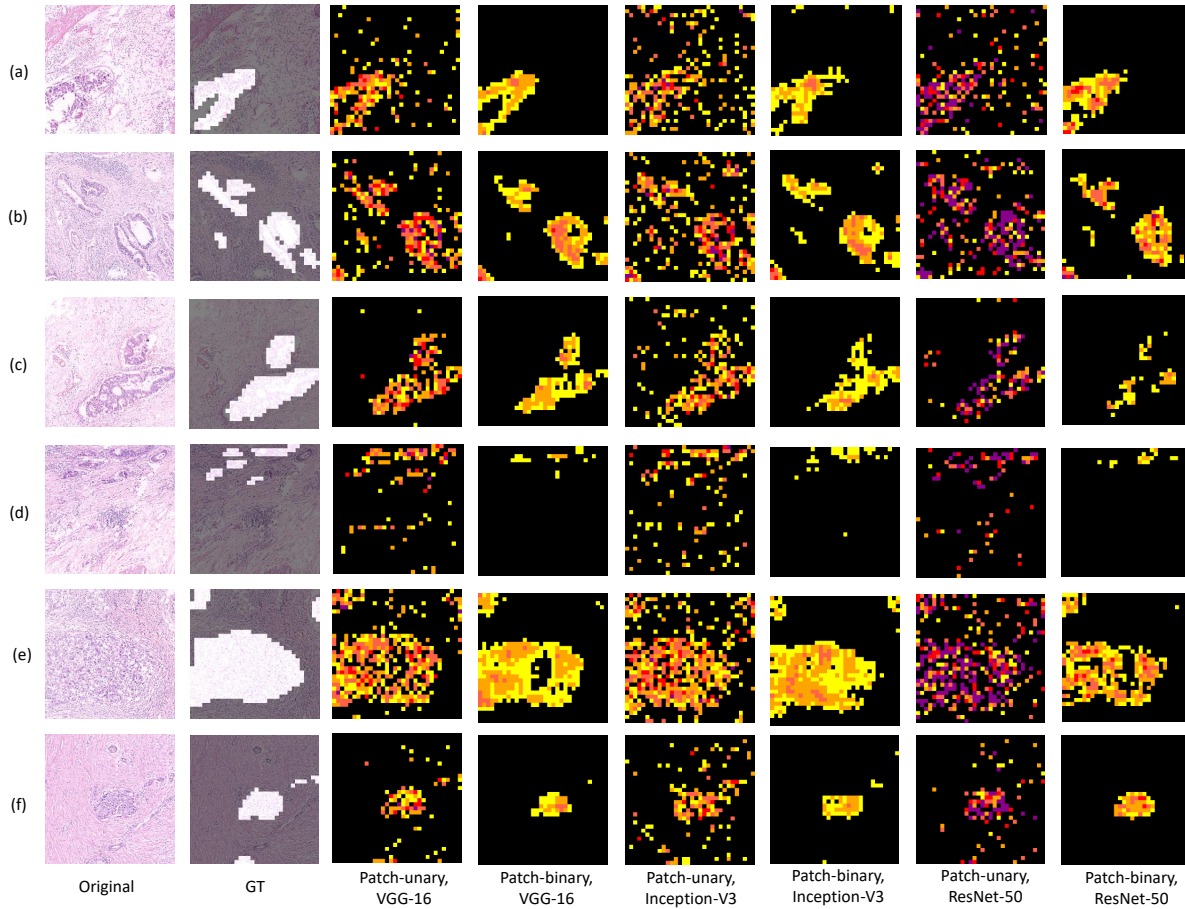


Fig 9 An example of the patch-level segmentation results of three CNNs on the validation set. The first and second columns show the original and their GT images. The third and fourth columns are the VGG-16 results, the fifth and sixth columns are the Inception-V3 results and the seventh and last columns are the ResNet-50 results.

From Fig. 9, we can find that the patch-binary segmentation can eliminate the noise vary effectively. However, it may change some correctly segmented regions in the patch-unary potential to wrong segmentation results. So, both the patch-unary and patch-binary potentials make sense in our HCRF model.

4.3.2 Optimization for Patch-unary and -binary Potentials

In order to further optimize the patch-unary and -binary segmentation results, we combine three patch-unary potentials and three patch-binary potentials to obtain one patch-unary potential and one patch-binary potential, respectively. Here, two optimization strategies are compared: The first is a direct “late fusion” strategy,⁴⁹ where the classification probabilities of the VGG-16, Inception-V3 and ResNet-50 networks are given weights with a 1:1:1 ratio and summed together to obtain a joint classification probability. The second is a grid optimization strategy,⁵⁰ where, based on our pre-tests, a step length of 0.05 is applied to give independent weights to the classification probabilities of the VGG-16, Inception-V3 and ResNet-50 networks. Additionally, in order to guarantee the image patch classification accuracy, we carry out the log operation to the probability. When we calculate the joint probability, this operation leads to a nonlinear case. So, in the optimized patch-level image segmentation results, we only use one pinkish-orange color to represent the positive regions and another black color to represent the negative regions.

Optimization for Patch-unary Potentials: For the patch-unary potentials, the weights by the grid optimization is shown in Table 6.

Table 6 The patch-unary weights of three CNNs using the grid optimization. The first row shows the CNNs. The second row shows the CNN weights.

CNN	VGG-16	Inception-V3	ResNet-50
Weight	0.55	0.25	0.20

From Table 6, we can find that, due to the VGG-16 network has a better image segmentation performance than that of other CNNs involved, it obtains the highest weight of 0.55. However, although the Inception-V3 and ResNet-50 networks have a weaker performance than the VGG-16, they still contribute to the final segmentation results, so they share the remaining weights with 0.25 and 0.20. Furthermore, an example of the optimized patch-unary segmentation results is shown in Fig. 10.

In Fig. 10, the grid optimization approach achieves a better image segmentation performance in details of the cancer regions. For more details, we give a comparison with the image patch classification confusion matrices in Fig. 11.

From Fig. 11, we can find that the grid optimization achieves a higher classification accuracy than that of the direct late fusion approach on both the foreground (0.7560) and background (0.7348) patches, as well it obtains a higher overall accuracy (0.7450) for all patches.

Optimization for Patch-binary Potentials: For the patch-binary potentials, the weights by the grid optimization is shown in Table 7.

Table 7 The patch-binary weights of three CNNs using the grid optimization. The first row shows the CNNs. The second row shows the weights.

CNN	VGG-16	Inception-V3	ResNet-50
Weight	0.40	0.00	0.60

From Table 7, we can find that, due to the ResNet-50 and VGG-16 networks have more robust image segmentation performance than that of the Inception-V3 network, they obtain 0.60 and 0.40 weights, respectively. However, because the Inception-V3 network has a much worse performance and it does not contribute any information to the final segmentation results, it is assigned a 0 weight. In addition, an example of the optimized patch-binary segmentation results is shown in Fig. 10.

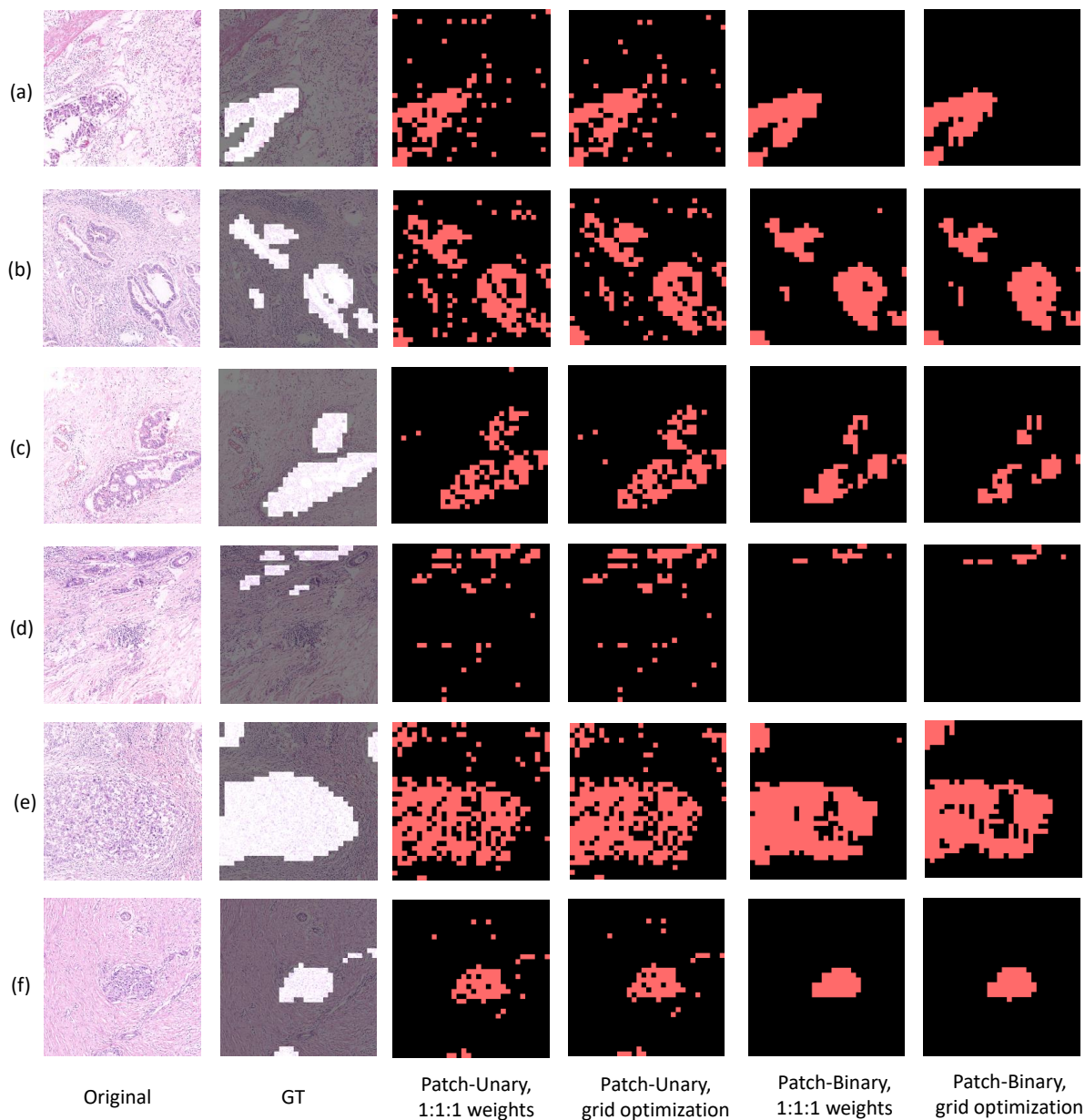


Fig 10 An example for the optimized patch-unary and patch-binary segmentation results on the validation set. The first and second columns show the original and their GT images, respectively. The third and fourth columns are the optimized patch-unary image segmentation results. In the third column, VGG-16, Inception-V3 and ResNet-50 networks have their patch-unary weights with a 1:1:1 ratio. In the fourth column, these three CNNs have their weights as shown in Table 6. The fifth and last columns are the optimized patch-binary image segmentation results. In the fifth column, VGG-16, Inception-V3 and ResNet-50 networks have their weights with a 1:1:1 ratio. In the last column, these three CNNs have their weights as shown in Table 7.

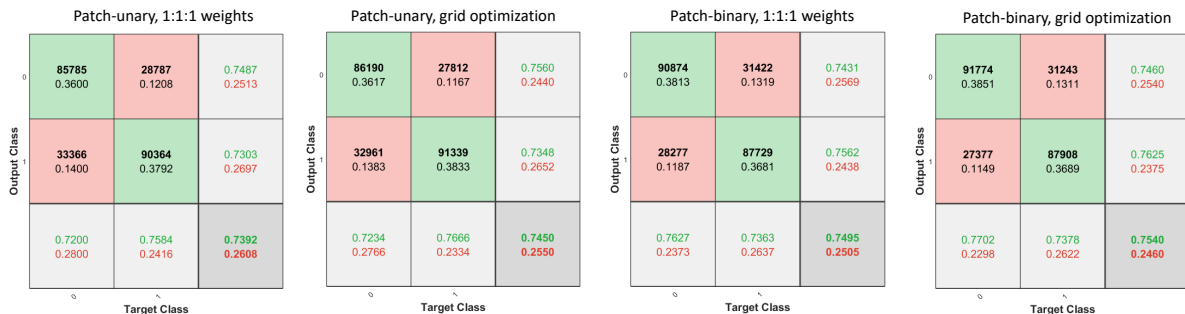


Fig 11 Image patch classification results of the optimized patch-unary and patch-binary potentials on the validation set. The first and second confusion matrices correspond to the 1:1:1 weighting and the grid optimization results of patch-unary potentials, respectively. The third and last confusion matrices correspond to the 1:1:1 weighting and the grid optimization results of patch-binary potentials, respectively. 1 represents positive and 0 represents negative.

In Fig. 10, the grid optimization strategy obtains a more clean image segmentation result, where more noise outside the cancer regions is removed. A comparison with the image patch classification confusion matrices is given in Fig. 11.

From Fig. 11, we can find grid optimization obtains a higher classification accuracy than that of the direct late fusion approach on the foreground (0.7460), background (0.7625) and all (0.7540) image patches.

4.4 Evaluation of the Proposed HCRF Model

4.4.1 Evaluation of the HCRF and Post-processing

Based on the pixel-level and patch-level image segmentation results in Sec. 4.2 and 4.3, the final result by the HCRF model is obtained, where we use the pixel-unary, pixel-binary, patch-unary and patch-binary segmentation accuracies as the weights to optimize the HCRF model. Specifically, because all of these four accuracies (0.7787, 0.7793, 0.7450 and 0.7540) are in $[0.7, 0.8]$ and lack of discrimination, and considering the computation efficiency of 2048×2048 pixels, we use them to minus 0.7 to enhance their distinction. Hence, we have the weights of 0.087, 0.0793, 0.0450 and 0.0540 for pixel-unary, pixel-binary, patch-unary and patch-binary potentials, respectively. In

addition, the segmentation result with the post-processing is also achieved. An example of the HCRF segmentation results is shown in Fig. 12.

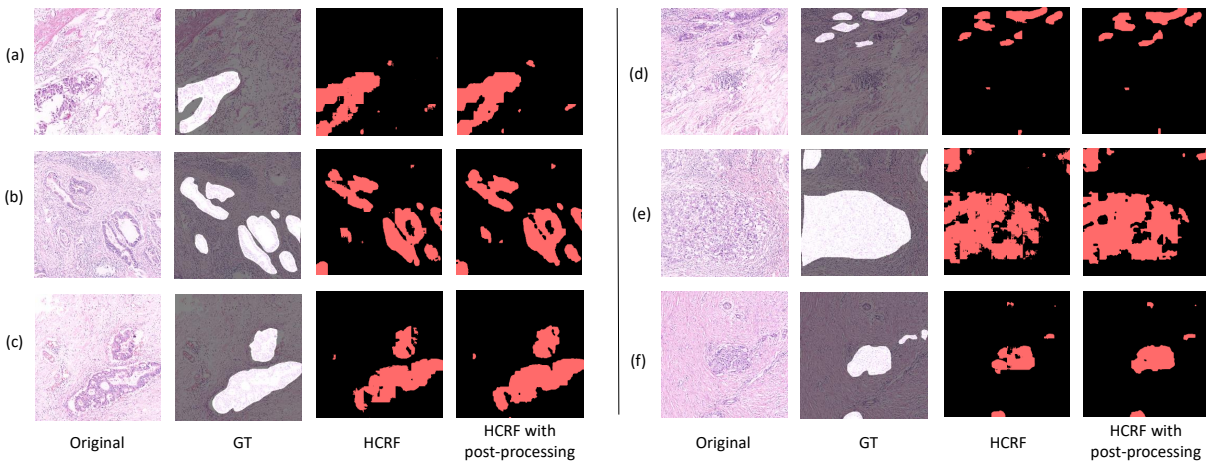


Fig 12 An example of the HCRF image segmentation results on the validation set. The first and second columns show the original and their GT images, respectively. The third and last columns are the HCRF image segmentation results and that with the post-processing.

From Fig. 12, we can find that the HCRF model achieves better image segmentation performance than that of the pixel-level potentials in Fig. 6, where the over-segmentation and under-segmentation cases are reduced. Specially, when the post-processing consisted of two steps which are MRF and morphological operation including once open operation is applied, the segmentation performance is further improved. In addition, the numerical evaluation for the HCRF segmentation performance is shown in Fig. 13.

From the comparison for seven evaluation criteria of the HCRF and HCRF with post-processing in Fig. 13, we can find that, four of them are improved (Dice, Specificity, RVD and Accuracy) and two of them are at nearly the same level (IoU and Precision). Hence, the HCRF with post-processing has as an overall improved image segmentation performance, and we choose it in our following experimental steps.

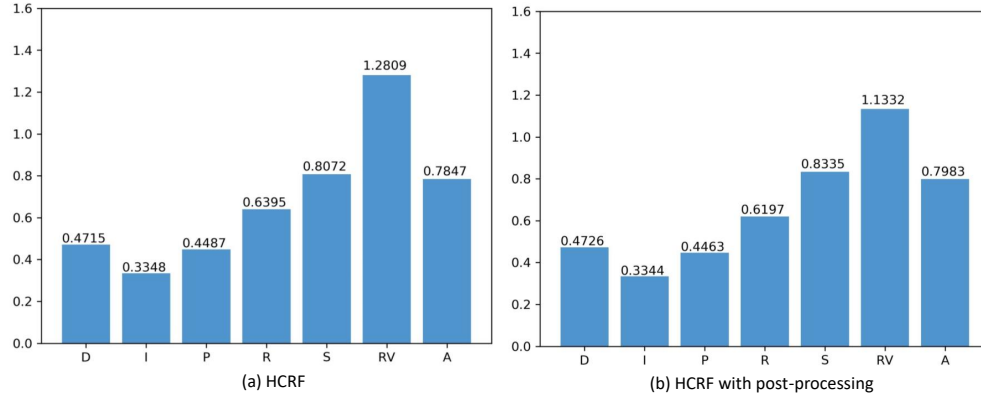


Fig 13 The evaluation for the image segmentation performance of the proposed HCRF model on the validation set. (a) and (b) are the evaluations of the proposed HCRF model and that with the post-processing on the validation set, respectively.

4.4.2 Evaluation of the HCRF Model on the Test Set

In order to prove the effectiveness of the proposed HCRF model (with the post-processing), we examine it on the test set, and an example of the segmentation results is shown in Fig. 14.

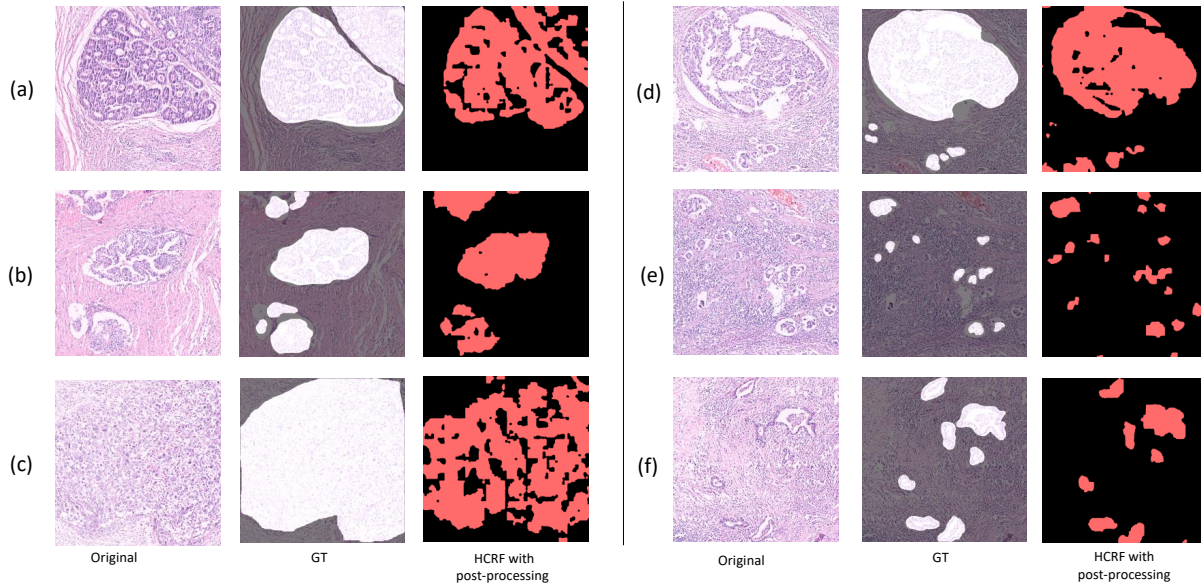


Fig 14 An example of the HCRF segmentation results on the test set. The first and middle columns show the original and GT images in the test set, respectively. The last column shows the image segmentation results by the proposed HCRF model (with the post-processing). (a) to (f) are six examples.

From Fig. 14, we can find that our HCRF model obtains good image segmentation results on the test set, where most of the positive (cancer) regions are segmented, and the edges of the regions

are smooth. Furthermore, a numerical evaluation for the HCRF segmentation performance on the test set is compared with that on the validation set in Fig. 15.

From the comparison in Fig. 15, we can find that although the test set has 280 images which are twice than the validation set, our proposed HCRF model also obtains good segmentation performance, where the values of all seven evaluation indexes on the test set are closed to that on the validation set, showing a high stability and a strong robustness of our method.

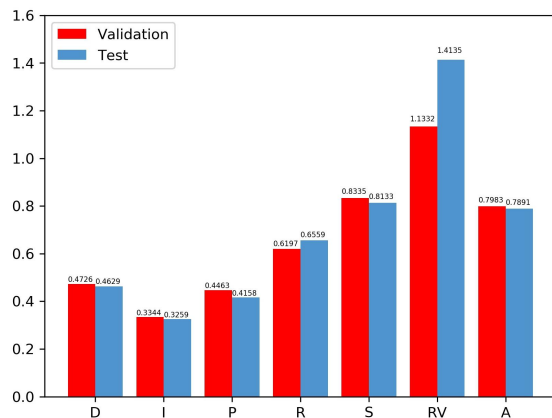


Fig 15 A comparison between the image segmentation performance of the proposed HCRF model with post-processing on the validation and test sets.

4.5 Comparison to Existing Methods

4.5.1 Existing Methods

In order to show the potential of the proposed HCRF method for the GHIS task, we compare it with seven existing methods, including three state-of-the-art methods (DenseCRF,⁵ SegNet⁵¹ and U-Net) and four classical methods (Otsu thresholding,⁵² Watershed,⁵³ k -means clustering⁵⁴ and MRF). The experimental settings of these existing methods are briefly introduced as follows:

- (1) The DenseCRF bases on U-Net features which is trained on the dataset in Table 2 and gets 2048×2048 images finally.
- (2) The U-Net is retrained on the dataset in Table 2 and gets 2048×2048

images finally. (3) The SegNet is retrained on the dataset in Table 2 and gets 2048×2048 images finally. (4) The Otsu thresholding method is used on the dataset in Table 1. (5) The Watershed algorithm is used with a two-stage way, where it is applied twice on the dataset in Table 1. (6) The k -means method is trained on the dataset in Table 1. (7) The MRF segmentation method is applied to the dataset in Table 1 and it includes two steps. First, we use k -means for clustering, then we use the MRF to the k -means result.

4.5.2 Image Segmentation Result Comparison

Fig. 16 shows an example of the segmentation results of our method and seven existing methods on the test set in Table 1.

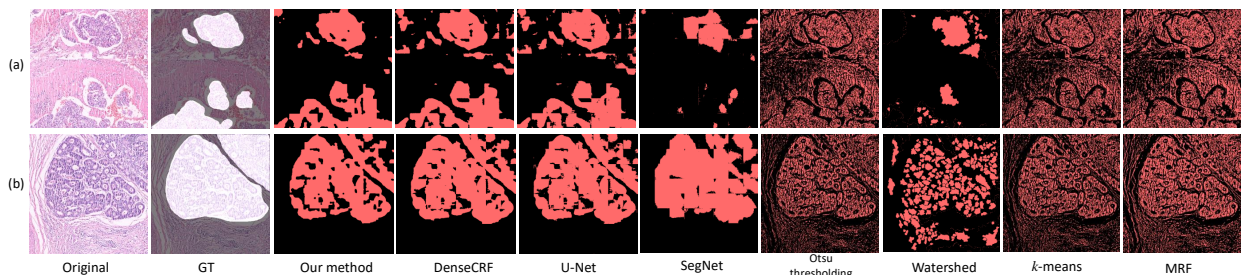


Fig 16 A comparison of the image segmentation results of our HCRF and other existing methods on the test set. The first and second columns show the original and GT images, respectively. The third shows the the results by our methods. Other columns show the results by other seven approaches.

From Fig. 16, we can find that our HCRF method has a better image segmentation performance than other existing methods in the visible comparison, where more positive regions (cancer) are correctly marked and less noise is remained. Furthermore, a numerical comparison between our HCRF method and other existing methods on the test set is given in Table 8.

From Table 8, we can find that: (1) Comparing to the state-of-the-art methods (DenseCRF, U-Net and SegNet), except Recall and Specificity, our HCRF behaves all better on other indexes. The Precision has more effectiveness to evaluate the foreground segmentation result and Recall has

Table 8 A numerical comparison of the image segmentation performance between our HCRF model and other existing methods. The first row shows different methods. The first column shows the evaluation criteria. The bold texts are the best performance for each criterion.

Criterion	Our HCRF	DenseCRF	U-Net	SegNet	Otsu thresholding	Watershed	<i>k</i> -means	MRF
Dice	0.4629	0.4578	0.4557	0.2008	0.2534	0.2613	0.2534	0.2396
IoU	0.3259	0.3212	0.3191	0.1300	0.1505	0.1585	0.1506	0.1432
Precision	0.4158	0.4047	0.4004	0.3885	0.2159	0.2930	0.2165	0.1839
Recall	0.6559	0.6889	0.6896	0.3171	0.4277	0.3541	0.4284	0.4991
Specificity	0.8133	0.7812	0.7795	0.8412	0.7082	0.7942	0.7078	0.5336
RVD	1.4135	1.6487	1.6736	2.0660	2.8859	1.9434	2.8953	4.5878
Accuracy	0.7891	0.7702	0.7684	0.7531	0.6598	0.7205	0.6593	0.5441

more effectiveness to evaluate the background segmentation result. When we focus on optimizing the foreground (the positive or abnormal regions), we get lower FP and higher Precision. Meantime the Recall is opposite to Precision. However, the Dice is a balance between the Precision and Recall, and our HCRF obtains the highest Dice value, showing an overall better image segmentation performance. From Fig. 16, we can find out that the SegNet may classify some abnormal areas to normal which leads to high TN, meantime, high Specificity. (2) Comparing to classical methods (Otsu thresholding, Watershed, *k*-means clustering and MRF), our HCRF model has better segmentation results. These classical methods have similar results, where they cannot separate entire abnormal areas, but get more unnecessary details in both normal and abnormal areas.

4.6 Mis-segmentation Analysis

Although our HCRF model achieves good gastric histopathology image segmentation performance, there is still a big gap of the mis-segmentation problems to overcome. To analyse the mis-segmentation reasons, we give an example in Fig. 17.

According to Fig. 17 and the medical knowledge from our cooperative histopathologists, the reason for image segmentation errors are as follows:

(1) From Fig. 17(a), we can find that the contents of the gastric histopathological images are complex, where the characteristics between normal and abnormal areas are not always obviously dif-

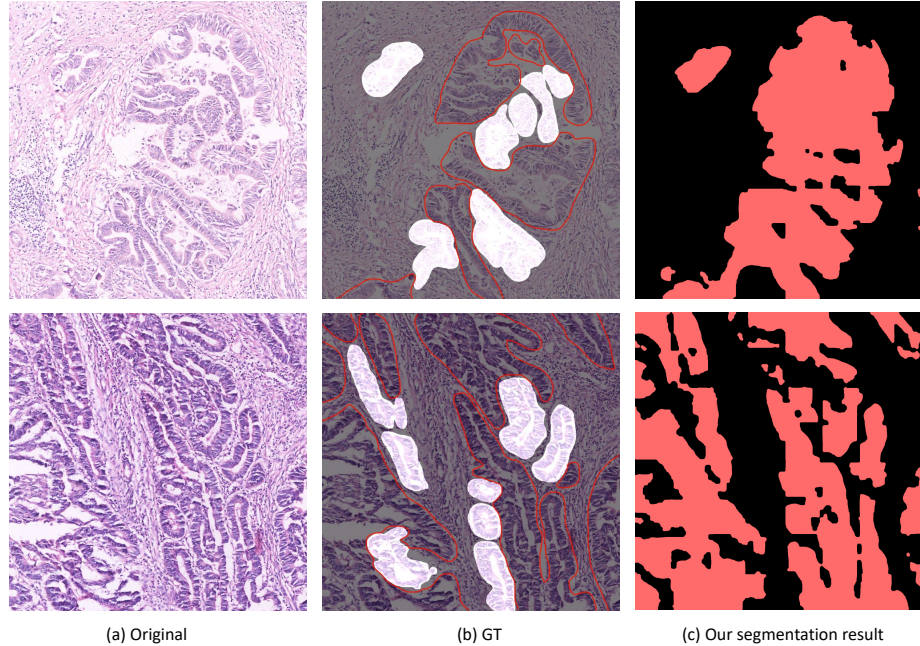


Fig 17 An example of the mis-segmentation results. (a) shows the original images. (b) denotes the GT images. (c) shows the mis-segmentation results. The regions in the red curves in (b) are the positive regions in the redrawn GT images.

ferent, leading to a difficulty in feature extraction or image content description.

(2) As shown in Fig. 17(b), when the abnormal regions in a gastric histopathological image are too many, the medical doctors drew the GT images roughly, where they did not figure out all of the abnormal regions. This low quality operation makes some positive regions to be labelled as negative, adding a training difficulty.

(3) From Fig. 17(b) and (c), we can find that, when we evaluate the segmentation results, our HCRF model may segment the positive regions correctly, but the original GT images may miss the corresponding regions. We consult our cooperative histopathologists and use red curves to redraw the regions that the original dataset did not label, where we can see that the original GT images in the applied dataset miss quite a lot of positive regions. It is obviously that the foreground of our segmentation result is more close to the redrawn GT images, but not the original GT images, and this case could lead to a low IoU and high SVD.

4.7 Computational Time

Finally, we briefly describe the computational time of our HCRF model. In our experiment, we use a workstation with Intel® Core™ i7-8700k CPU 3.20GHz, 32GB RAM and GeForce RTX 2080 8GB. When we retrain the U-Net and fine-tune the VGG-16, Inception-V3 and ResNet-50 networks, we use Keras framework fore-end and Tensorflow framework back-end. Table 9 shows the retraining time of the U-Net and fine-tuning time of the VGG-16, Inception-V3 and ResNet-50 networks.

Table 9 The training time of four CNNs using 140 training and 140 validation images.

CNN	U-Net	VGG-16	Inception-V3	ResNet-50
Time/hours	37.7	10.0	6.1	5.6

Furthermore, Table 10 shows the testing time of our HCRF model on 280 images (2048×2048 pixels) within two working stages. The first stage is the “Main Body” of the HCRF model, which is the stage from Layer I to Layer V in Fig. 2. The second stage is the “Post-processing” stage, which denotes Layer VI in Fig. 2. For histopathologists in the practical work, if they want a faster segmentation result, they can just run the Main Body stage of our HCRF model; if they want a more accurate segmentation result, they can run the whole HCRF model with the post-processing stage.

Table 10 The testing time of our HCRF on 280 gastric histopathology images.

Time	Main Body	Post-Processing	Sum
Total Time/hours	2.2	2.7	4.9
Mean Time/seconds	28.1	33.5	61.6

5 Conclusion and Future Work

In this paper, we propose a HCRF model to the gastric histopathology image segmentation task. This HCRF model not only uses traditional unary and binary potentials, but also applies higher order potentials to improve the segmentation quality. In pixel-level potentials, we retrain the U-Net; in patch-level potentials, we fine-tune the VGG-16, Inception-V3 and ResNet-50 networks. Furthermore, when jointing the pixel-level and patch-level potentials, we use different weights for different potentials to optimize the model. In the experiment, the proposed HCRF method is finally tested on a gastric H&E histopathological test set and obtains a 78.91% segmentation accuracy, which is nearly close to the 79.83% segmentation accuracy on the validation set, showing the robustness and potential of our method.

In the future work, we plan to add more higher potentials, such as object detection potentials³⁸ to improve the segmentation quality. Meanwhile, we will add other state-of-the-art CNNs with different structures for more accurate segmentation results to our HCRF model.

Disclosures

The authors declare that there are no conflicts of interest related to the research presented in this article.

Acknowledgments

This work is supported by the “National Natural Science Foundation of China” (No. 61806047), the “Fundamental Research Funds for the Central Universities” (No. N171903004, N180719020), “Scientific Research Fund of Sichuan Provincial Science & Technology Department” (No. 2017TD0019),

and “Scientific Research Fund of Chengdu Science and Technology Bureau” (No. 2017-GH02-00049-HZ, 2018-YF05-00981-GX).

References

- 1 B. Stewart and C. Wild, *World Cancer Report 2014*, World Health Organization, (UN) (2014).
- 2 E. Garcia *et al.*, “Automatic Lymphocyte Detection on Gastric Cancer IHC Images Using Deep Learning,” in *Proc. of CBMS 2017*, 200–204 (2017).
- 3 K. Simonyan and A. Zisserman, “Very Deep Convolutional Networks for Large-scale Image Recognition,” *arXiv:1409.1556* (2014).
- 4 J. Long, E. Shelhamer, and T. Darrell, “Fully Convolutional Networks for Semantic Segmentation,” in *Proc. of ICPR 2015*, 3431–3440 (2015).
- 5 L. Chen *et al.*, “DeepLab: Semantic Image Segmentation with Deep Convolutional Nets, Atrous Convolution, and Fully Connected CRFs,” *IEEE Transactions on Pattern Analysis and Machine Intelligence* **40**(4), 834–848 (2018).
- 6 L. Hou *et al.*, “Patch-based Convolutional Neural Network for Whole Slide Tissue Image Classification,” in *Proc. of CVPR 2016*, 2424–2433 (2016).
- 7 S. Li, “Markov Random Field Models in Computer Vision,” in *Proc. of ECCV 1994*, 361–370 (1994).
- 8 R. Gonzalez, R. Woods, and S. Eddins, *Digital Image Processing Using MATLAB*, Pearson Education, India (2004).
- 9 H. Sharma *et al.*, “A Multi-resolution Approach for Combining Visual Information Using Nuclei Segmentation and Classification in Histopathological Images,” in *Proc. of VISAPP 2015*, 37–46 (2015).

- 10 T. Elsheikh *et al.*, “American Society of Cytopathology Workload Recommendations for Automated Pap Test Screening: Developed by the Productivity and Quality Assurance in the Era of Automated Screening Task Force,” *Diagnostic Cytopathology* **41**(2), 174–178 (2013).
- 11 Y. LeCun, Y. Bengio, and G. Hinton, “Deep learning,” *Nature* **521**(7553), 436 (2015).
- 12 R. Lozano, “Comparison of Computer-assisted and Manual Screening of Cervical Cytology,” *Gynecologic Oncology* **104**(1), 134–138 (2007).
- 13 N. Kumar *et al.*, “A Dataset and a Technique for Generalized Nuclear Segmentation for Computational Pathology,” *IEEE Transactions on Medical Imaging* **36**(7), 1550–1560 (2017).
- 14 Y. Cui *et al.*, “A Deep Learning Algorithm for One-step Contour Aware Nuclei Segmentation of Histopathological Images,” *arXiv:1803.02786* (2018).
- 15 J. Lafferty, A. McCallum, and F. Pereira, “Conditional Random Fields: Probabilistic Models for Segmenting and Labeling Sequence Data,” in *Proc. of ICML 2001*, 282–289 (2001).
- 16 X. He, R. Zemel, and M. Carreira-Perpiñán, “Multiscale Conditional Random Fields for Image Labeling,” in *Proc. of CVPR 2004*, **2**, 1–8 (2004).
- 17 F. Sha and F. Pereira, “Shallow Parsing with Conditional Random Fields,” in *Proc. of HLT-NAACL 2003*, 134–141 (2003).
- 18 B. Settles, “Biomedical Named Entity Recognition Using Conditional Random Fields and Rich Feature Sets,” in *Proc. of JNLPBA 2004*, 104–107 (2004).
- 19 K. Chang *et al.*, “Analysis and Prediction of the Critical Regions of Antimicrobial Peptides Based on Conditional Random Fields,” *PloS One* **10**(3), e0119490 (2015).
- 20 J. Ruiz-Sarmiento *et al.*, “UPGMpp: A Software Library for Contextual Object Recognition,” in *Proc. of REACTS 2015*, 1–14 (2015).

- 21 Y. Wang and J. Rajapakse, "Contextual Modeling of Functional MR Images with Conditional Random Fields," *IEEE Transactions on Medical Imaging* **25**(6), 804–812 (2006).
- 22 Y. Artan *et al.*, "Prostate Cancer Localization with Multispectral MRI Using Cost-Sensitive Support Vector Machines and Conditional Random Fields," *IEEE Transactions on Image Processing* **19**(9), 2444–2455 (2010).
- 23 S. Park *et al.*, "Domain-Specific Image Analysis for Cervical Neoplasia Detection Based on Conditional Random Fields," *IEEE Transactions on Medical Imaging* **30**(3), 867–878 (2011).
- 24 D. Mary, V. Anandan, and K. Srinivasagan, "An Effective Diagnosis of Cervical Cancer Neoplasia by Extracting the Diagnostic Features Using CRF," in *Proc. of ICCEET 2012*, 563–570 (2012).
- 25 S. Kosov *et al.*, "Environmental Microorganism Classification Using Conditional Random Fields and Deep Convolutional Neural Networks," *Pattern Recognition* **77**, 248–261 (2018).
- 26 C. Li *et al.*, "Cervical Histopathology Image Classification Using Multilayer Hidden Conditional Random Fields and Weakly Supervised Learning," *IEEE Access* **7**(1), 90378–90397 (2019).
- 27 O. Ronneberger, P. Fischer, and T. Brox, "U-net: Convolutional Networks for Biomedical Image Segmentation," in *Proc. of MICCAI 2015*, 234–241 (2015).
- 28 C. Szegedy *et al.*, "Going Deeper with Convolutions," in *Proc. of ICPR 2015*, 1–9 (2015).
- 29 S. Ioffe and C. Szegedy, "Batch Normalization: Accelerating Deep Network Training by Reducing Internal Covariate Shift," *arXiv:1502.03167* (2015).
- 30 C. Szegedy *et al.*, "Rethinking the Inception Architecture for Computer Vision," in *Proc. of ICPR 2016*, 2818–2826 (2016).

- 31 K. He *et al.*, “Deep Residual Learning for Image Recognition,” in *Proc. of ICPR 2016*, 770–778 (2016).
- 32 T. Falk *et al.*, “U-net: Deep learning for cell counting, detection, and morphometry,” *Nature Methods* **16**(1), 67 (2019).
- 33 Ö. Çiçek *et al.*, “3D U-Net: Learning Dense Volumetric Segmentation from Sparse Annotation,” in *Proc. of MICCAI 2016*, 424–432 (2016).
- 34 J. Hammersley and P. Clifford, “Markov Fields on Finite Graphs and Lattices.” Unpublished manuscript (1971).
- 35 R. Gupta, “Conditional Random Fields.” Unpublished Report, IIT Bombay (2006).
- 36 S. Zheng *et al.*, “Conditional Random Fields as Recurrent Neural Networks,” in *Proc. of ICCV 2015*, 1–17 (2015).
- 37 V. Vineet, J. Warrell, and P. Torr, “Filter-based Mean-field Inference for Random Fields with Higher-Order Terms and Product Label-spaces,” in *Proc. of ECCV 2002*, 1–14 (2012).
- 38 A. Arnab *et al.*, “Higher Order Conditional Random Fields in Deep Neural Networks,” in *Proc. of ECCV 2016*, 524–540 (2016).
- 39 O. Russakovsky *et al.*, “Imagenet Large Scale Visual Recognition Challenge,” *International Journal of Computer Vision* **115**(3), 211–252 (2015).
- 40 Y. Matsumoto *et al.*, “Kobe University, NICT and University of Siegen on the TRECVID 2016 AVS Task,” in *Proc. of TRECVID 2016*, 1–8 (2016).
- 41 S. Kumar and M. Hebert, “Discriminative Random Fields,” *International Journal of Computer Vision* **68**(2), 179–201 (2006).

- 42 D. Kermany *et al.*, “Identifying Medical Diagnoses and Treatable Diseases by Image-based Deep Learning,” *Cell* **172**(5), 1122–1131 (2018).
- 43 Z. Zhang *et al.*, “Pathological Image Classification of Gastric Cancer based on Depth Learning,” *Computer Science* **45**(11A), 263–268 (2018).
- 44 A. Garcia-Garcia *et al.*, “A Review on Deep Learning Techniques Applied to Semantic Segmentation,” *arXiv:1704.06857* (2017).
- 45 H. Chang *et al.*, “Performance Measure Characterization for Evaluating Neuroimage Segmentation Algorithms,” *Neuroimage* **47**(1), 122–135 (2009).
- 46 A. Taha and A. Hanbury, “Metrics for Evaluating 3D Medical Image Segmentation: Analysis, Selection, and Tool,” *BMC Medical Imaging* **15**(1), 29 (2015).
- 47 P. Christ *et al.*, “Automatic Liver and Tumor Segmentation of CT and MRI Volumes Using Cascaded Fully Convolutional Neural Networks,” *arXiv:1702.05970* (2017).
- 48 D. Powers, “Evaluation: from Precision, Recall and F-measure to ROC, Informedness, Markedness and Correlation.” Technical Report in School of Informatics and Engineering, Flinders University, Adelaide, Australia, No. SIE-07-001 (2011).
- 49 C. Snoek, M. Worring, and A. Smeulders, “Early versus Late Fusion in Semantic Video Analysis,” in *Proc. of MM 2005*, 1–4 (2005).
- 50 M. Ingber and A. Mitra, “Grid Optimization for the Boundary Element Method,” *International Journal for Numerical Methods in Engineering* **23**(11), 2121–2136 (1986).
- 51 V. Badrinarayanan, A. Kendall, and R. Cipolla, “Segnet: A Deep Convolutional Encoder-decoder Architecture for Image Segmentation,” *IEEE Transactions on Pattern Analysis and Machine Intelligence* **39**(12), 2481–2495 (2017).

- 52 N. Otsu, "A Threshold Selection Method from Gray-level Histograms," *IEEE Transactions on Systems, Man, and Cybernetics* **9**(1), 62–66 (1979).
- 53 L. Vincent and P. Soille, "Watersheds in Digital Spaces: An Efficient Algorithm based on Immersion Simulations," *IEEE Transactions on Pattern Analysis and Machine Intelligence* **13**(6), 583–598 (1991).
- 54 J. Hartigan and M. Wong, "Algorithm AS 136: A k -means Clustering Algorithm," *Journal of the Royal Statistical Society. Series C (Applied Statistics)* **28**(1), 100–108 (1979).

Changhao Sun received his B.E. degree in communication engineering from the Northeastern University, China, in 2018. Currently, he is a Master Student in the Research Group for Microscopic Image and Medical Image Analysis in the Northeastern University, China. His research interests are gastric histopathology image segmentation, conditional random fields and deep learning.

Chen Li received his Dr.-Ing. degree from the University of Siegen (1.0 score, MAGNA CUM LAUDE), Germany in 2016. From 2016 to 2017, he worked as a Postdoctoral Researcher in the Johannes Gutenberg University Mainz, Germany. Currently, he is working as an Associate Professor in the Northeastern University, China. His research interests are microscopic image analysis, machine learning, pattern recognition, machine vision, multimedia retrieval and membrane computing.

Xiaoyan Li received her Ph.D. degree in Pathology from China Medical University, China, in 2014. From 2014 till now, she works in the Department of Pathology, Cancer Hospital of China Medical University, Liaoning Cancer Hospital and Institute, engaged in the diagnosis of surgical

tumor pathology and molecular pathology, and her main research direction is the occurrence and development mechanism of breast cancer and cervical cancer.